AGU ADVANCING EARTH AND SPACE SCIENCES

JGR Space Physics

RESEARCH ARTICLE
10.1029/2023JA031486

Key Points:

- Long-period disturbance emerged in New Zealand ~1 hr prior to the arrival of the atmospheric Lamb wave, and propagated at ~0.6 km/s and ~0.4 km/s toward southwest
- Repeated passages of the atmospheric Lamb wave caused suites of internal gravity waves, propagating at ~0.3 km/s
- Atmospheric mode of ~3.7 mHz became stronger ~14 hr after eruption in New Zealand

Supporting Information:

Supporting Information may be found in the online version of this article.

Correspondence to:

D. D. Wijaya,
dudy.wijaya@itb.ac.id

Citation:

Muafiry, I. N., Wijaya, D. D., Meilano, I., & Heki, K. (2023). Diverse ionospheric disturbances by the 2022 Hunga Tonga-Hunga Ha'apai eruption observed by a dense GNSS array in New Zealand. *Journal of Geophysical Research: Space Physics*, *128*, e2023JA031486. https://doi.org/10.1029/2023JA031486

Received 16 MAR 2023
Accepted 16 OCT 2023

Author Contributions:

Conceptualization: Ihsan Naufal Muafiry
Data curation: Ihsan Naufal Muafiry
Formal analysis: Ihsan Naufal Muafiry, Dudy D. Wijaya
Funding acquisition: Dudy D. Wijaya, Irwan Meilano
Investigation: Ihsan Naufal Muafiry, Irwan Meilano
Methodology: Kosuke Heki
Project Administration: Dudy D. Wijaya, Irwan Meilano
Software: Kosuke Heki
Supervision: Dudy D. Wijaya, Irwan Meilano, Kosuke Heki
Validation: Dudy D. Wijaya, Irwan Meilano, Kosuke Heki
Visualization: Ihsan Naufal Muafiry, Kosuke Heki

Diverse Ionospheric Disturbances by the 2022 Hunga Tonga-Hunga Ha'apai Eruption Observed by a Dense GNSS Array in New Zealand

Ihsan Naufal Muafiry[1,2], Dudy D. Wijaya[1], Irwan Meilano[1], and Kosuke Heki[3,4]

[1]Faculty of Earth Sciences (FITB), Institut Teknologi Bandung (ITB), Bandung, Indonesia, [2]Research Center for Climate and Atmosphere, National Research and Innovation Agency (BRIN), Bandung, Indonesia, [3]Shanghai Astronomical Observatory, Chinese Academy of Science, Shanghai, China, [4]Hokkaido University, Sapporo, Japan

Abstract Using a network of global navigation satellite systems receivers in New Zealand, located 2,000–3,300 km southwest of Hunga Tonga-Hunga Ha'apai volcano, we found at least three different kinds of ionospheric disturbances from changes in total electron contents (TEC). Ionospheric signatures of the near-field acoustic wave propagating ~0.8 km/s were not clear in New Zealand due possibly to large geometric decay. The first disturbance emerged ~1 hr after the eruption and traveled toward southwest with a speed of ~0.6 km/s. This, together with the subsequent disturbance propagating by ~0.4 km/s, suggests its link to the ahead-of-tsunami ionospheric disturbance, excited by the Lamb wave and subsequent tsunamis traveling in the Pacific Ocean. The second disturbance started ~2 hr after the eruption as tens of waves with periods 10–15 min propagating by ~0.3 km/s, possibly internal gravity waves (IGW) excited by the passages of the Lamb wave. Such IGW wave trains continued until ~10 hr after the eruption. The Lamb wave traveled round the earth, and its second and third passages disturbed the ionosphere in New Zealand on the next day as similar IGW wave trains following the Lamb wave. The third disturbance occurred as an enhancement of the harmonic oscillation of TEC with frequency of ~3.7 mHz, ~14 hr after the eruption. This might be an atmospheric mode excited by the eruption, but its propagation and sudden activation remain unexplained.

1. Introduction

The phase differences of microwave signals in two frequency bands from global navigation satellite systems (GNSS) can be used to measure ionospheric total electron contents (TEC). TEC provides useful information on upper-atmospheric dynamics related to space weather. Past observations have also caught various ionospheric disturbances caused by events in the solid earth such as large earthquakes and strong volcanic eruptions.

Large earthquakes generate acoustic waves (AW) in the atmosphere. They propagate upward and make N-shaped signatures in TEC time-series ~10 min after earthquakes as coseismic ionospheric disturbances (e.g., Heki, 2021). They propagate by ~0.8 km/s, the AW speed at the F region. Ionospheric disturbances by volcanic eruptions occur in two different forms, that is, harmonic oscillations of TEC (e.g., Heki & Fujimoto, 2022) and N-shaped pulses like coseismic disturbances (e.g., Cahyadi et al., 2021). They occur after continuous Plinian eruptions and Vulcanian explosions, respectively.

The Hunga Tonga-Hunga Ha'apai (HTHH) eruption started ~4:15 UT on 15 January 2022, as one of the largest volcanic eruptions with the highest plume ever recorded (Carr et al., 2022). Ionospheric responses to this event have been reported in lots of articles. From regional GNSS receivers, Astafyeva et al. (2022) found the sequence of N-shaped TEC changes, excited by multiple explosions possibly synchronized with the atmospheric mode (Tarumi & Yoshizawa, 2023). Themens et al. (2022) analyzed global GNSS-TEC data and found ionospheric responses to the passage of the Lamb Wave (LW) propagating worldwide along the surface by ~0.3 km/s. Regional GNSS-TEC observations detected multiple passages of LW in Japan (Heki, 2022), China (Li et al., 2023), and in Indonesia (Muafiry et al., 2022). Conjugate ionospheric anomalies were found to propagate in two hemispheres simultaneously by Themens et al. (2022) and were further studied by Lin et al. (2022).

Here we focus on ionospheric response to the HTHH eruption, recorded by ground GNSS stations in New Zealand. They serve as the closest dense GNSS network to HTHH. Dense networks allow us to constrain propagation speeds of ionospheric disturbances and offer a unique opportunity to study different kinds of disturbances caused by this eruption. We also compare the TEC data with the atmospheric pressure data from the nationwide

Writing – original draft: Ihsan Naufal Muafiry
Writing – review & editing: Dudy D. Wijaya, Irwan Meilano, Kosuke Heki

array of surface barometers in New Zealand to discuss causal relationship between the LW passages and the ionospheric disturbances.

2. GNSS-TEC Data

We downloaded GNSS data from Land Information New Zealand (LINZ), the dense network of GNSS receivers in New Zealand (https://www.linz.govt.nz/). We converted them to slant TEC (STEC) time series following procedures described in Heki (2021). The 42 GNSS stations shown in Figure 1 record two L-band microwave carrier phases from American (GPS) and Russian (GLONASS) GNSS every 30 s. From STEC, we removed satellite and station inter-frequency biases from global ionospheric map (GIM) header information and converted it to vertical TEC (VTEC) by multiplying with cosine of the incidence angle of the line-of-sights into a thin layer at 300 km altitude. The inter-frequency biases of receivers not included in GIM headers are removed using the minimum scalloping method (Rideout & Coster, 2006).

Figure 1 shows time series over the whole 15 January 2022, at the AUCK station in northern New Zealand. We express TEC in TEC unit (1 TECU = 10^{16} electrons/m^2). Themens et al. (2022), as a part of data from global GNSS stations, reported TEC changes in New Zealand. In our study. We perform more detailed analyses of different kinds of ionospheric disturbances in this region, taking advantage of a dense network deployed within a relatively short distance from HTHH.

Figure 2 compares the TEC time series obtained at seven different stations with three GPS satellites G10, G24, G32. Figures 2a–2c shows VTEC time series from seven stations at various distances from HTHH. The initial disturbance, with a period of ∼30 min, arrived shortly after 5 UT at the station nearest to HTHH, and propagated to farther stations. After 6 UT, numbers of waves with periods 10–15 min propagated toward southwest over New Zealand. The initial longer-period disturbances seem to propagate faster than the later shorter-period wave trains. However, one would find it difficult to separate components with different periods and propagation velocities in Figure 2. In the next section, we try to identify various waves by plotting the data in different ways.

3. Ionospheric Disturbances in New Zealand Due To the HTHH Eruption

3.1. First Disturbance Ahead of the LW Arrival

Figure 2 is not useful for constraining the propagation velocities of different components. To extract ionospheric oscillations with specific periods by the HTHH eruption, we use wavelet transformation (Heki et al., 2022). Its period was set either to 30 min or 12 min, to extract the long-term initial disturbances and shorter-term signatures in later periods, respectively. This helps us identify propagation velocities of different waves. Here we also compare GNSS-TEC data with the LW signatures in surface pressure to study their causal relationship. Figures 3a–3c expresses the wavelet-transformed VTEC data using colors and plots them as a function of the distance of SIP from HTHH (vertical axis) and time (horizontal axis). We assumed a thin layer of 300 km altitude to calculate SIP positions (we will justify this altitude later in Section 4.3). There are 102 barometer station used in this study installed in New Zealand (Gusman et al., 2022). In Figure 3d, we plot surface atmospheric pressure data in a similar manner to TEC.

Figures 3a–3c shows the wavelet transform of GNSS-TEC data using satellites G23, G10, and G32 over a few hours period shortly after the HTHH eruption. Please note that we used the wavelet period 30 min for G23 and G10 and 12 min for G32, to highlight components with those periods. The time windows of Figures 3a–3c are slightly shifted to show periods of the highest elevation of the three satellites.

We first confirm that we do not see the ∼0.8 km/s component due to the propagation of the direct AW from HTHH. Such waves decays rapidly with distance, that is, New Zealand would not be close enough to HTHH to record this component. In UT 5.0–5.5, positive ionospheric anomalies were detected to propagate with the velocity of ∼0.6 km/s (Figures 3a and 3b). They arrived earlier than the first passage of LW (L1) in the barometer records (Figure 3d) by ∼1 hr. These properties do not match any types of known ionospheric disturbances caused by large earthquakes and volcanic eruptions. Origin of these components would be discussed in detail later in Section 4.1.

3.2. Second TEC Changes Associated With the Passages of LW

The blue dashed line in Figure 3d indicates the slope and arrival times expected from the propagation speed 0.3 km/s for LW. It clearly overlaps with the pressure anomaly from barometer records in 6–7 UT. Figure 3c

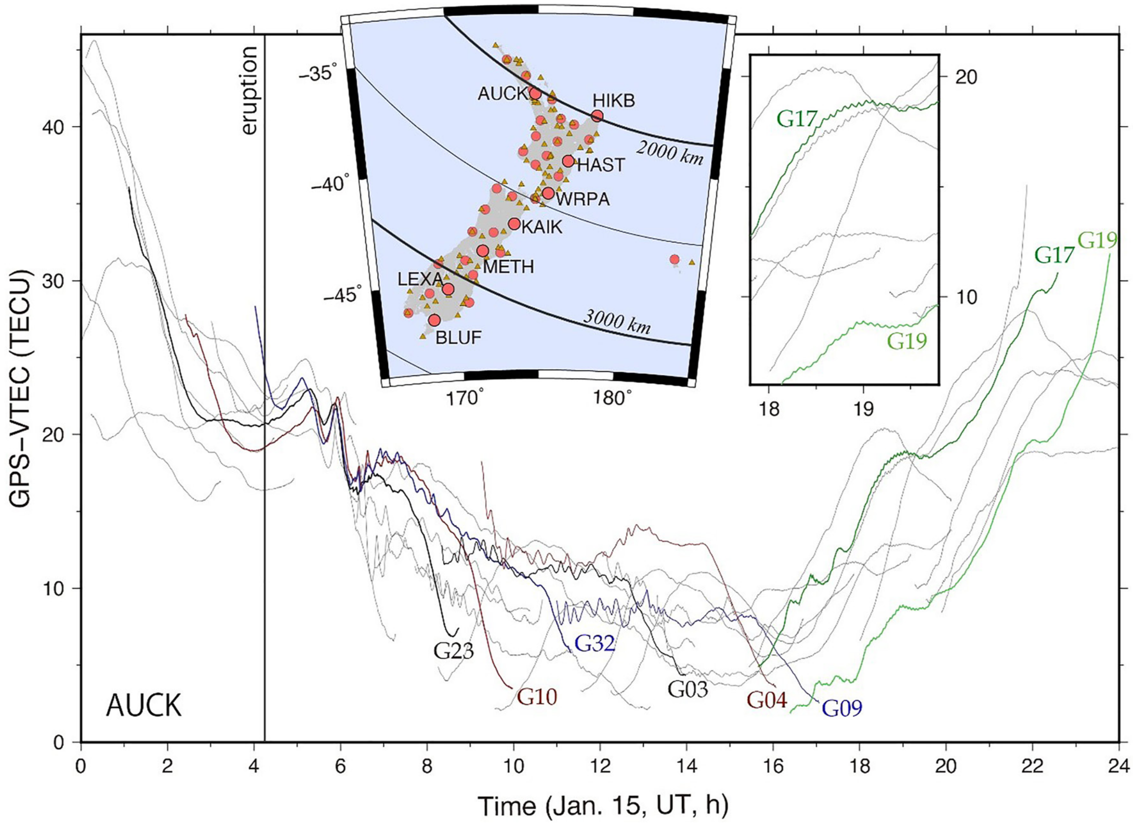

Figure 1. VTEC time series on 2022 January 15 at the AUCK station, Auckland, northern New Zealand. The total electron contents (TEC) data from three GPS satellites, G10, G 23, and G32, are used to study initial ionospheric signatures of the eruption. Then, satellites G03, G04, and G09 are used to study passages of internal gravity waves 6–12 hr after the eruption. We then study atmospheric mode signatures in the data with G17 and G19, ~14 hr after the eruption. Inset map shows the global navigation satellite systems stations in New Zealand (circles) and surface atmospheric pressure sensors (triangles). Distance contours from HTHH are also shown. The part 17.8–19.8 UT is enlarged in the inset to emphasize the small amplitude harmonic oscillation of TEC.

shows lots of waves with periods 10–15 min started propagating toward southwest by ~0.3 km/s immediately after the LW passage. They would be internal gravity waves (IGW) which was excited by LW near surface and propagated upward. In the simulation by Kherani et al. (2016), they call it co-tsunami ionospheric disturbances (CTID), although it was LW in the present case rather than propagating tsunamis that excited them.

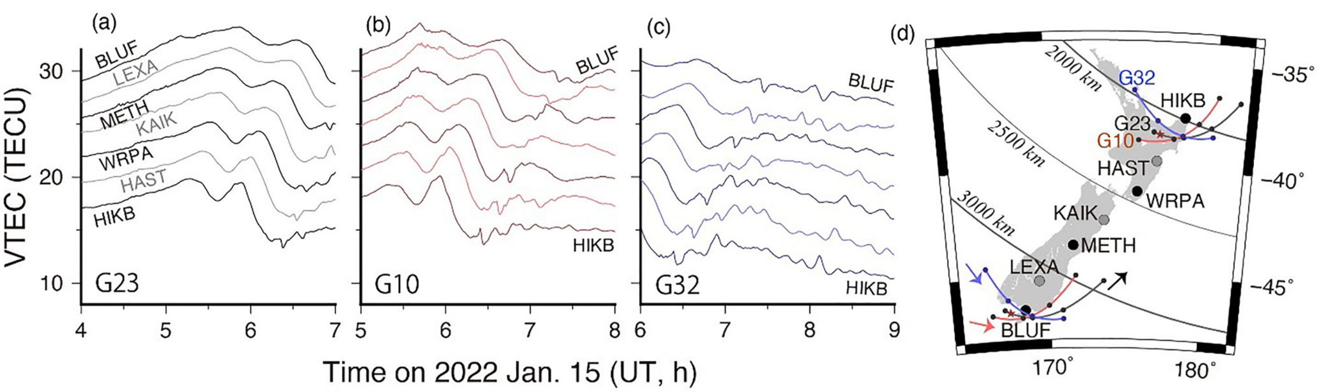

Figure 2. VTEC plots at seven global navigation satellite systems stations with distances 2,000–3,300 km from HTHH using satellites G23 (a), G10 (b), and G32 (c), for 3 hr periods 4–7 (a), 5–8 (b), and 6–9 (c) UT. The numbers in the vertical axis indicate VTEC values at HIKB, and we added artificial biases to other stations for visual clarity. The map (d) shows the station positions together with the SIP trajectory of the three satellites from HIKB and BLUF stations during the periods shown in (a–c). Small dots on the SIP tracks indicate 1 hr time marks.

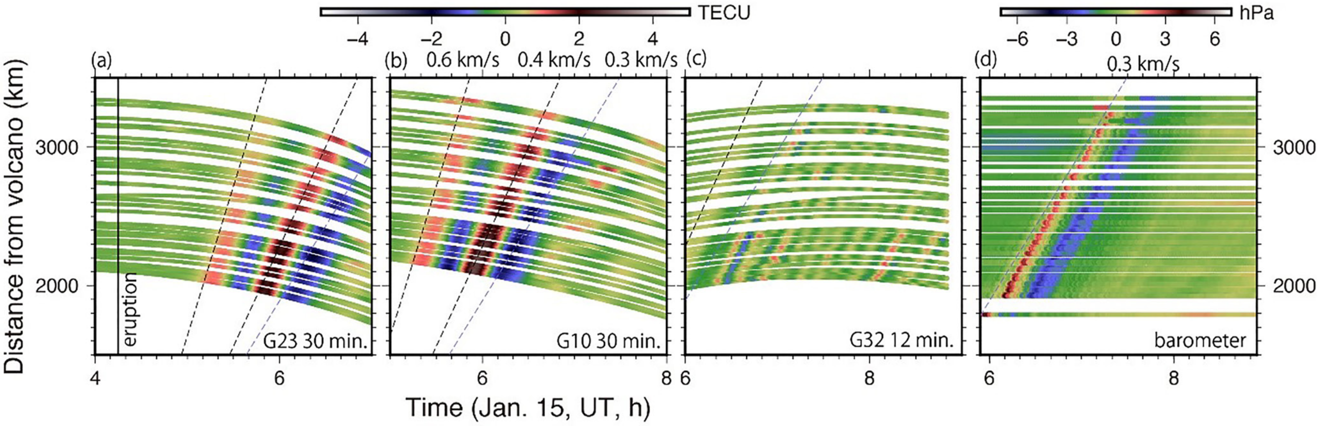

Figure 3. Ionospheric disturbances extracted with 30 min (a, b) and 12 min (c) wavelet, obtained using GPS satellites 23, 10, and 32, respectively, plotted as a function of time (horizontal axis) and distance from HTHH (vertical axis). LW signals are recorded in the ground barometer array as a component propagating by ~0.3 km/s (d).

According to earlier reports, the ionospheric signatures of the LW traveling round the earth several times were observed in Japan (Heki, 2022), Indonesia (Muafiry et al., 2022), and in China (Li et al., 2023). Here we look for those signals in New Zealand. Figure 4d indicates that the second LW passage (L2) occurred 12–13 UT on the next day (January 16), ~2 hr earlier than the time expected assuming 0.3 km/s throughout its path. The slope for L2 is negative as the wavefront moves from southwest to northeast.

Figures 4a–4c shows ionospheric disturbances propagating toward northeast caused by L2. Although they are weaker than the first passage by nearly an order of magnitude, they have similar characteristics, that is, they have periods of 10–15 min and propagate immediately after LW by the same velocity. Thus, they would have been excited by similar processes as the L1-induced disturbances shown in Figure 3c. In Figure 4c, in addition to components propagating toward northeast, we can see weak components propagating toward southwest by ~0.2 km/s. These are the continuation of the disturbances caused by tsunami, discussed at the end of this section.

Figure 5 shows the disturbances associated with the third passage of LW (L3) at 18–19 UT, January 16, ~5 hr after its second passage. Again, ionospheric disturbances appear as IGW propagating by ~0.3 km/s immediately after the passages of LW. Ionospheric disturbances by L2 and L3 are weaker than L1 by nearly an order of magnitude although the amplitude of the surface pressure changes in L2 and L3 are only ~1/2 of L1. This would be partly due to the lower background VTEC (Figure S1 in Supporting Information S1) during L2 and L3 reflecting different local times. Small amplitude disturbances traveling toward northeast (i.e., with negative slopes) overlap with the L3 signatures in Figures 5a–5c. Considering the local time and season, they would be the summer night type MSTID (medium-scale traveling ionospheric disturbances) (Otsuka et al., 2011).

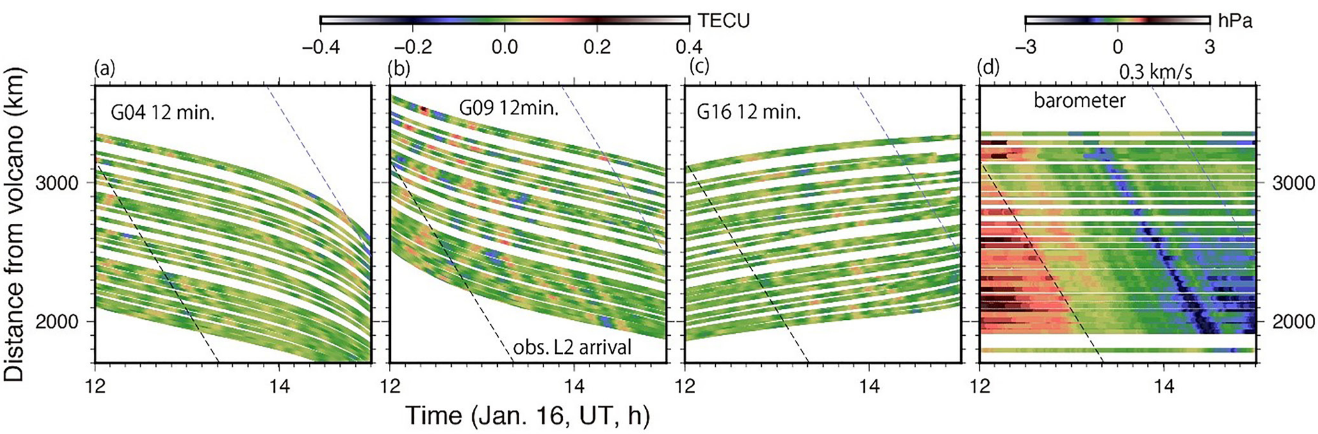

Figure 4. Ionospheric disturbances by L2 extracted with 12 min wavelet as a function of time on 16 January 2022, and distance from HTHH. We used GPS satellites 4 (a), 9 (b), and 16 (c). L2 signals recorded in the ground barometer array (d) indicates that the observed arrivals (thick dashed lines in black) are ~2 hr earlier than those expected from 0.3 km/s (thin dashed lines in blue).

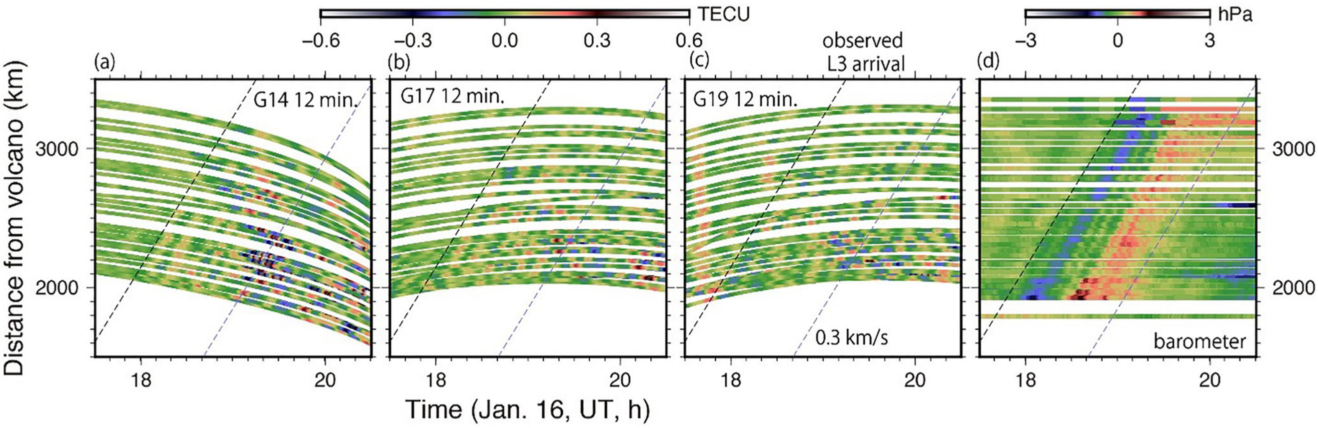

Figure 5. Ionospheric disturbances by L3 extracted with 12 min wavelet as a function of time on 16 January 2022, and distance from HTHH, observed using GPS satellites 14 (a), 17 (b), and 19 (c). L3 signals recorded in the ground barometer array are shown in (d). Their arrivals are ~1.5 hr earlier than those expected from 0.3 km/s.

Numbers of IGW, with periods of 10–15 min, followed the initial passage of LW on the day of the eruption. Here, we show that such IGW wave train continued to travel over New Zealand until ~14 UT, ~10 hr after the eruption (Figure 6, partly visible in Figure 4b). Those shortly after the LW passage around 6 UT would have been excited by pressure changes near the surface. Those arriving later would also have been excited by tsunami propagating in the Pacific Ocean behind the LW pulse. In fact, the first tsunami arrived at ~7 UT in northern New Zealand and smaller tsunamis continued as seen in a tide gauge record (Figure 7a). Their excitation mechanisms would be similar to co-tsunami traveling ionospheric anomalies (CTID) by Kherani et al. (2016).

One important feature is that they show propagation velocity of ~0.3 km/s, faster than the typical tsunami propagation speed of 0.20–0.22 km/s. Some waves propagate with this slower speed, for example, around 12.5 UT at distances ~2,000 km from HTHH (Figure 6c). In the surface atmospheric pressure (Figure 7b), we see mixture of pressure anomalies passing over New Zealand with 0.2 and 0.3 km/s. The time series of sea surface height at a tide gauge station in north-eastern New Zealand (Figure 7a) shows an arrival of large amplitude tsunami around 12 UT, and it might be responsible for the ionospheric disturbance propagating by ~0.2 km/s around 12.5 UT. We still do not know the exact proportion of the contribution from LW and tsunami to the wave train during this

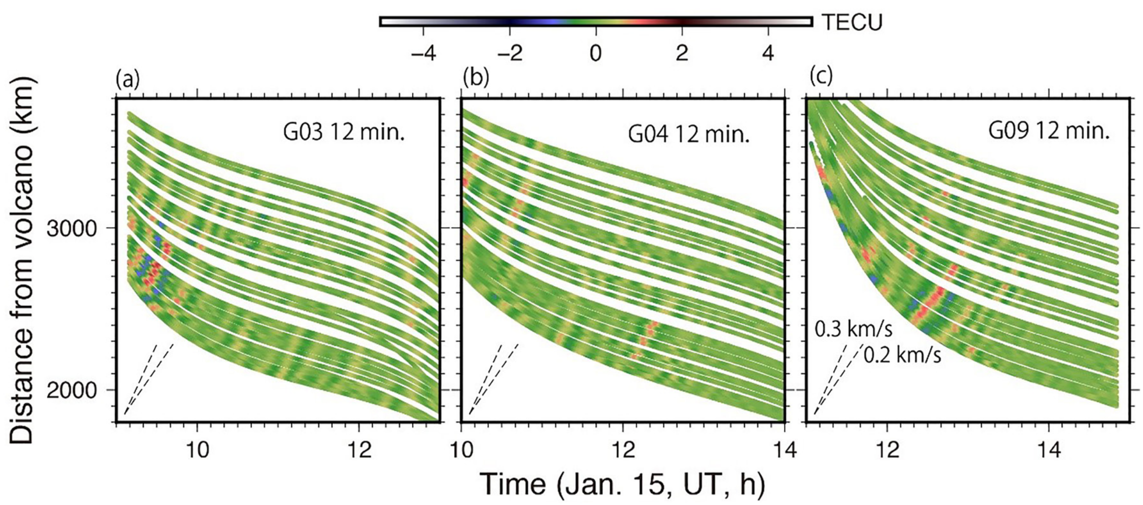

Figure 6. Ionospheric disturbances extracted with 12 min wavelet as a function of time on 15 January 2022, 9–15 UT, about 5–9 hr after the eruption. They propagate by ~0.3 km/s, but slower speeds (~0.2 km/s) are seen occasionally, for example, around 12–13 UT. Internal gravity waves wave train passing over New Zealand disappears around 14 UT (~10 hr after eruption), and the ionosphere remains calm until the enhancement of atmospheric modes around 18 UT. Dashed lines indicate 0.2 and 0.3 km/s slope.

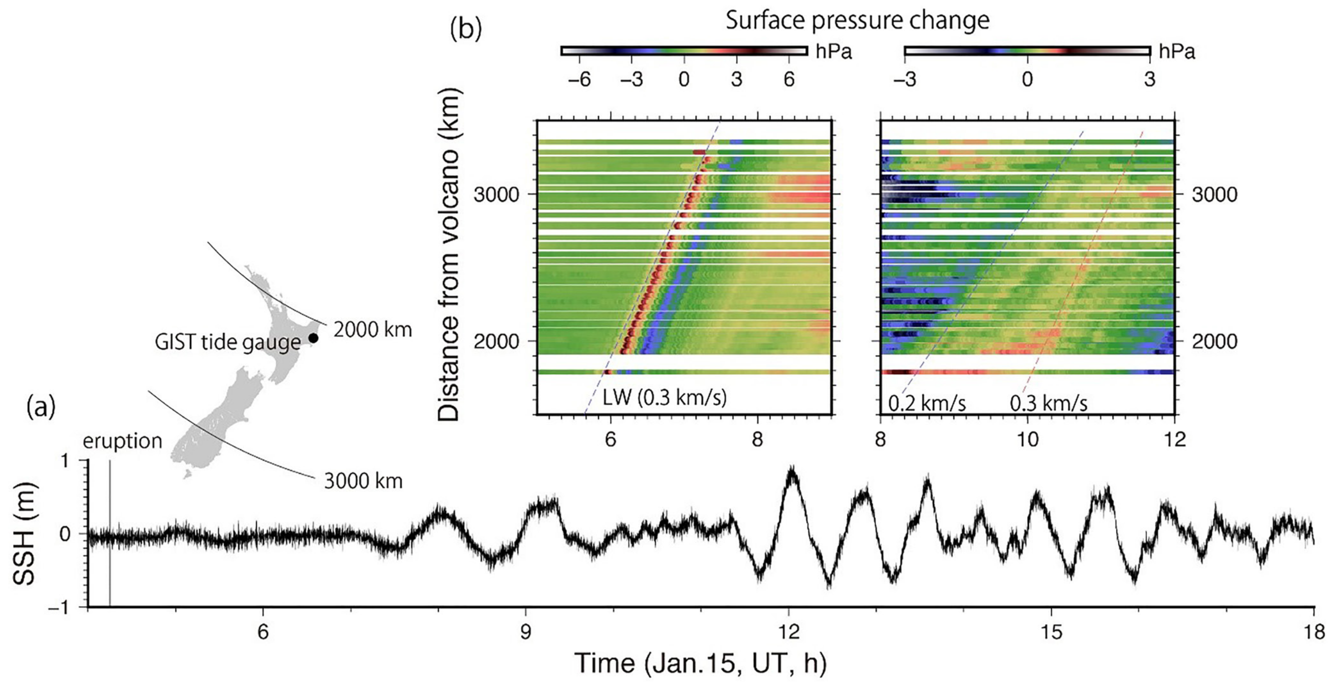

Figure 7. (a) Sea surface height at the GIST tide gauge, northeast New Zealand, on 15 January 2022. Tsunami continues throughout the studied period. Two small circles in the map indicate distance of 2,000 and 3,000 km from HTHH. (b) Surface atmospheric pressure anomalies in two periods (5–9 UT and 8–12 UT) plotted as the function of time and distance from the volcano. In the first period, the strong LW signature prevails. In the second period, numbers of weaker waves pass over New Zealand in two different velocities, 0.2 km/s and 0.3 km/s, possibly related to tsunami and LW, respectively.

period. By around 14 UT, IGW signatures almost disappear, and the ionosphere above New Zealand becomes calm.

3.3. Enhancement of an Atmospheric Mode as the Third Disturbance

In the period approximately 18–19 UT, harmonic oscillation of TEC is observed in several satellites including G17 and G19, highlighted in Figure 1 inset. The TEC time series after removing long period components by fitting polynomials are given in Figure 8. Such harmonic TEC oscillations are commonly seen during Plinian eruptions as reviewed in Cahyadi et al. (2020). However, they occurred only during the eruptions, and emergence of such oscillations 14–15 hr after the eruption is exceptional. Also, the spatial extent of such oscillations in past cases have been limited within a few hundreds of kilometers around the volcano. Therefore, it is also exceptional that such oscillations are found in the region with distances beyond 2,000 km from the volcano. This will be discussed in detail in Section 4.2.

4. Discussions

4.1. Origin of the Initial Component

Figures 3a and 3b shows that components propagating by ∼0.6 km/s arrived significantly earlier than LW. These velocities are much slower than AW velocities in the F region of the ionosphere (∼0.8 km/s) and are significantly faster than IGW (0.2–0.3 km/s). Thanks to the dense GNSS array in New Zealand, these velocities are well constrained. It is difficult to attribute them either to direct AW or IGW from HTHH, and we need something else to explain their physical mechanism.

Ahead-of-tsunami ionospheric disturbances (ATID) were found in numerical simulation for the 2011 Tohoku-oki earthquake by Kherani et al. (2016) and detected after the 2004 Sumatra-Andaman earthquake as a component propagating at ∼0.6 km/s by Bagiya et al. (2017). They are caused by acoustic gravity waves excited by tsunami propagating by ∼0.25 km/s in an open ocean. They arrive ∼20–60 min prior to the tsunami at epicentral distances

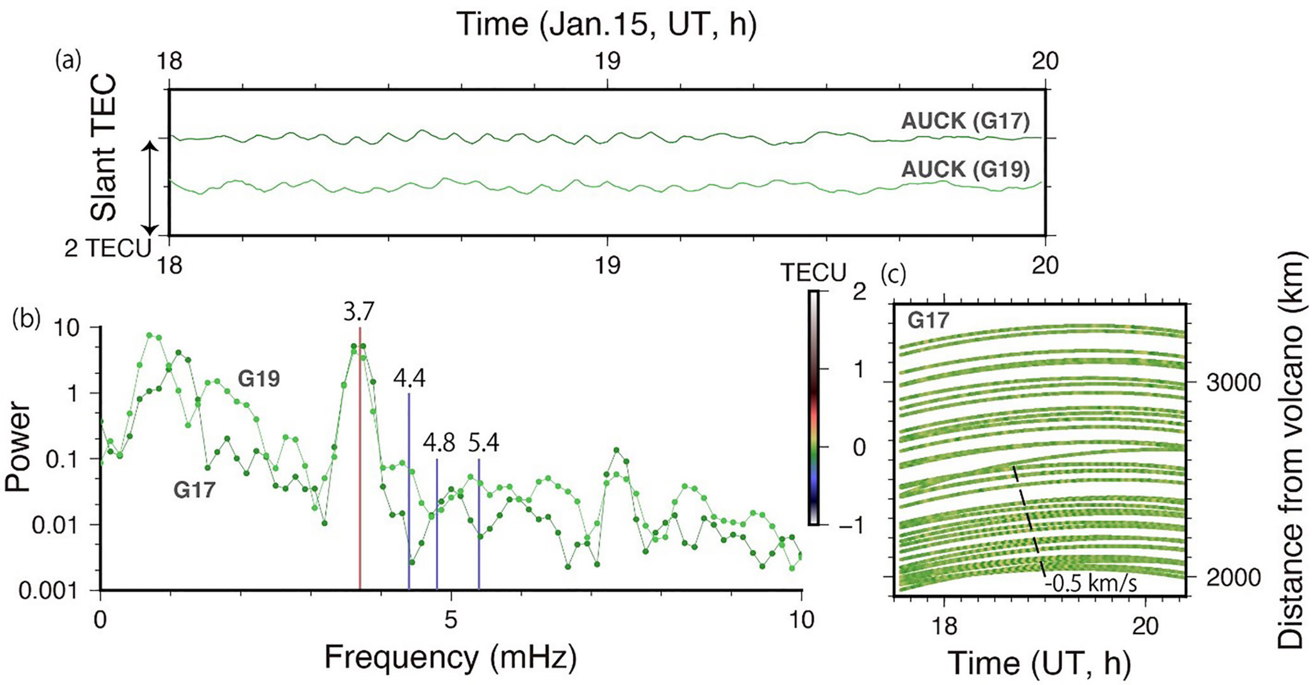

Figure 8. (a) Harmonic oscillation of total electron contents from two satellites, G17 and G19, observed at AUCK. We removed the best-fit degree nine polynomials to isolate short period components. In (b), we show frequency components obtained by the Blackman-Tukey method in the same way as Heki and Fujimoto (2022). Only the 3.7 mHz component (period: ∼270 s) is strong, and the other three peaks are not clear. (c) Time-distance plot for all the stations in New Zealand for the G17 signals after 270 s wavelet transformation. They appear to propagate at 0.5 km/s toward the volcano.

6–12°. Considering the velocity and earlier arrival, we speculate that the initial disturbance found in New Zealand is caused by ATID.

Kherani et al. (2016) assumed propagating tsunamis as the source. Here, however, we further speculate that surface atmospheric pressure disturbances caused by the propagating LW would play the same role. They may have excited ATID arriving ∼1 hr prior to the LW passage as the "ahead-of-Lamb-wave" ionospheric disturbances for the region with distance of 2,000 km or more.

Following the passage of the first ∼0.6 km/s component, the second disturbance with a similar period propagate with a slightly slower velocity of ∼0.4 km/s (Figures 3a and 3b). As seen in Figure 4 of Kherani et al. (2016), ATID is composed of multiple waves with slightly different propagation velocities, and we suspect this also a part of ATID. This speculation owes much to the lack of known disturbances having the observed properties. Hence, our interpretation needs to be modified when future studies clarified other physical mechanisms for the component propagating at 0.6 km/s from a volcano.

4.2. Harmonic Oscillation in 18–19 UT

During the Plinian eruption of the Fukutoku-Okanoba submarine volcano in 2021 August, Heki and Fujimoto (2022) identified four frequency peaks corresponding to atmospheric modes and their overtones. Spectrum analysis results, given in Figure 8b, show only the fundamental mode of ∼3.7 mHz and no other frequency peaks. Such oscillations are also known to propagate outward from the volcano by ∼0.8 km/s, the acoustic wave velocity in the F region (Cahyadi et al., 2020; Heki & Fujimoto, 2022; Nakashima et al., 2016).

Taking advantage of the dense array in New Zealand, we can see how such oscillatory signals propagate in space. Figure 8c shows that the harmonic oscillation signals do not propagate from the volcano by the prescribed velocity (0.8 km/s). If we focus on the distance range 2,000–2,500 km, the oscillation signal seems to move "toward" the volcano by ∼0.5 km/s. Obviously, the origin and dynamics of the atmospheric oscillation signals need further studies using all available data outside New Zealand. Because this is out of the scope of the present study, we leave it as a future issue and just report its behavior within New Zealand here.

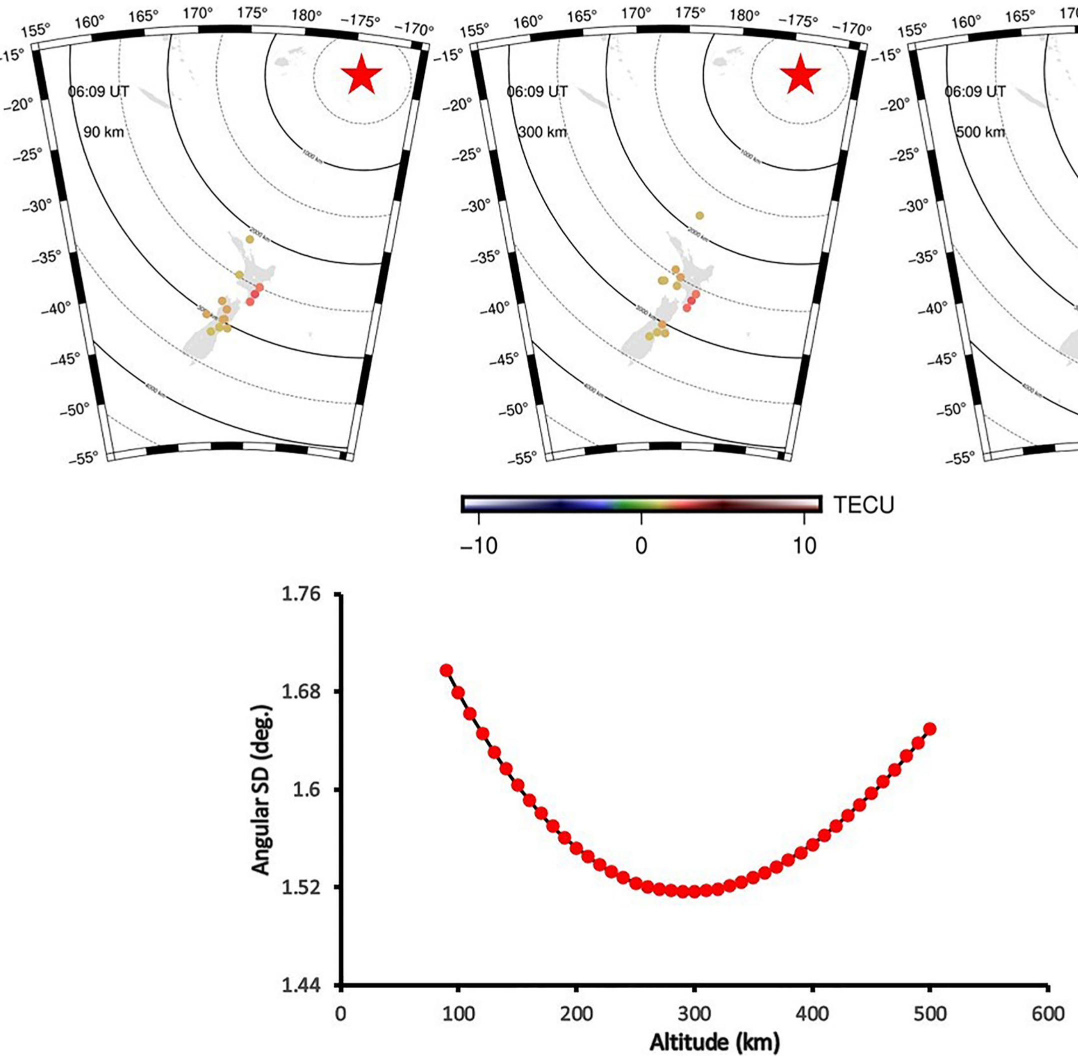

Figure 9. Result of minimum angular SD of SIP in New Zealand at 6:09 UT, January 15, when the strongest positive anomalies occur in the northeastern global navigation satellite systems stations. We used satellites G10, G18, G21 and R15, R22, and eight stations LKTA, METH, MQZQ, MTJO, DNVK, HAST, WRPA, and AUCK.

4.3. Height of the Ionospheric Disturbances

Electrons around the altitude of 300 km are mainly responsible for various ionospheric disturbance. Sometimes, those in the E region (altitude ∼100 km) makes strong irregularities, like sporadic-E, as shown by Muafiry et al. (2018) using three-dimensional tomography. We here clarify the height of ionospheric electron density anomalies caused by the HTHH eruption by a simple method used in He and Heki (2016). We first calculate angular standard deviation (SD) of SIPs showing anomalies on the same wavefront, and then minimizing it by tuning the height of the anomalies.

Here we used the SIP with eight stations in New Zealand and five GPS and GLONASS satellites in northeastern-southwestern skies (i.e., distributed perpendicular to the wavefront) at the epoch 06:09 UT showing large positive anomalies propagating at ∼0.4 km/s. Here we demonstrate that the SIPs of satellite-station pairs concentrate most tightly by assuming the height of ∼300 km (Figure 9). We also constrained the height of the ionospheric disturbance due to the 2022 HTHH eruption in Indonesia (Muafiry et al., 2022), and the result (Figure S2 in Supporting Information S1) showed a good agreement with the New Zealand case.

International Reference Ionosphere (IRI2016, Bilitza et al., 2017) suggests that the ionospheric electron density at the studied time in New Zealand had its maximum at height 290–300 km. This confirms that the altitude ranges with high electron density govern ionospheric disturbances even though the disturbance originates from phenomena near the surface.

5. Concluding Remarks

This study revealed diverse nature of ionospheric disturbances caused by a large volcanic eruption. This was made possible by a dense array in New Zealand located relatively close to the volcano. Observations are summarized, in the sequence of time, as follows,

1. There were no signatures of direct AW from HTHH,.
2. Iinitial disturbance with a period ~30 min propagated by ~0.6 and ~0.4 km/s and arrived ~1 hr prior to LW.,
3. The wave train of short-period (10–15 min) IGW propagated by ~0.3 km/s following the passage of LW.,
4. The wave train of CTID propagating by 0.2–0.3 km/s until ~10 hr after the eruption.
5. Transient enhancement of atmospheric modes was found ~14 hr after the eruption.
6. LW that traveled over New Zealand repeatedly on the next day of the eruption also caused IGW wave trains.

Within these six, (3) and (4) are not clearly separable, and (6) is the repetition of the same phenomena as (3). For the waves in (2), we speculate they were excited as ATID (Kherani et al., 2016) by LW. There were two additional passages of LW on the next day. However, such ATID-like disturbances were not observed. On the other hand, the IGW wave trains were triggered by all the three passages of LW, which clearly demonstrated their causal relationship.

In past eruptions, atmospheric modes were observed in terms of harmonic oscillations of TEC. However, they are all found within a few hundreds of kilometers from the volcanoes. In the present case, we detected enhancement of such oscillations at distances exceeding 2,000 km from the volcano.

Data Availability Statement

The authors thank Meteorological Service of New Zealand Ltd (Dr. Chris Noble) for providing surface pressure data (Gusman et al., 2022). Also, we thank the University of Berne (aiub.unibe.ch/CODE) for GIM. The GNSS receiver data were downloaded from Land Information New Zealand (https://www.geodesy.linz.govt.nz/positionz/?page=text) and coastal tide gauge data (GNS Science, 2022) were provided by geonet (https://tilde.geonet.org.nz/ui/data-exploration). Plots were created using Generic Mapping Tools (GMT) version 6 (Wessel et al., 2019) licensed version 3 or later, available at https://www.genericmapping-tools.org/.

Acknowledgments
We thank the anonymous reviewer for constructive comments. This study was supported by the Lembaga Penelitian dan Pengabdian Masyarakat-Institut Teknologi Bandung (LPPM-ITB) under ITB Research Grant 2023 and also by the Postdoctoral Program of Faculty of Earth Sciences (FITB), Institut Teknologi Bandung, Indonesia (No. 1607C/IT1.C01/KS.00/2022). KH is supported by President's International Fellowship Initiative of Chinese Academy of Sciences (Grant 2022VEA0014).

References

Astafyeva, E., Maletckii, B., Mikesell, T. D., Munaibari, E., Ravanelli, M., Coïsson, P., et al. (2022). The 15 January 2022 Hunga Tonga eruption history as inferred from ionospheric observations. *Geophysical Research Letters*, *49*(10), e2022GL098827. https://doi.org/10.1029/2022GL098827

Bagiya, M. S., Kherani, E. A., Sunil, P. S., Sunil, A. S., Sunda, S., & Ramesh, D. S. (2017). Origin of the ahead of tsunami traveling ionospheric disturbances during Sumatra tsunami and offshore forecasting. *Journal of Geophysical Research: Space Physics*, *122*(7), 7742–7749. https://doi.org/10.1029/2017JA023971

Bilitza, D., Altadill, D., Truhlik, V., Shubin, V., Galkin, I., Reinisch, B., & Huang, X. (2017). International reference ionosphere 2016: From ionospheric climate to real-time weather predictions. *Space Weather*, *15*(2), 418–429. https://doi.org/10.1002/2016SW001593

Cahyadi, M. N., Handoko, E. Y., Rahayu, R. W., & Heki, K. (2021). Comparison of volcanic explosions in Japan using impulsive ionospheric disturbances. *Earth Planets and Space*, *73*(1), 228. https://doi.org/10.1186/s40623-021-01539-5

Cahyadi, M. N., Rahayu, R. W., Heki, K., & Nakashima, Y. (2020). Harmonic ionospheric oscillation by the 2010 eruption of the Merapi volcano, Indonesia, and the relevance of its amplitude to the mass eruption rate. *Journal of Volcanology and Geothermal Research*, *405*, 107047. https://doi.org/10.1016/j.jvolgeores.2020.107047

Carr, J. L., Horváth, Á., Wu, D. L., & Friberg, M. D. (2022). Stereo plume height and motion retrievals for the record-setting Hunga Tonga-Hunga Ha'apai eruption of 15 January 2022. *Geophysical Research Letters*, *49*(9), e2022GL098131. https://doi.org/10.1029/2022GL098131

Gns Science (2022). GeoNet Aotearoa New Zealand coastal tsunami gauge digital waveform dataset [Dataset]. GNS Science, GeoNet. https://doi.org/10.21420/EJ6W-RC96

Gusman, A. R., Roger, J., Noble, C., Wang, X., Power, W., & Burbridge, D. (2022). The 2022 Hunga Tonga-Hunga Ha'apai volcano air-wave generated tsunami. *Pure and Applied Geophysics*, *179*(10), 3511–3525. https://doi.org/10.1007/s00024-022-03154-1

He, L., & Heki, K. (2016). Three-dimensional distribution of ionospheric anomalies prior to three large earthquakes in Chile. *Geophysical Research Letters*, *43*(14), 7287–7293. https://doi.org/10.1002/2016GL069863

Heki, K. (2022). Ionospheric signatures of repeated passages of atmospheric waves by the 2022 Jan. 15 Hunga Tonga-Hunga Ha'apai eruption detected by QZSS-TEC observations in Japan. *Earth Planets and Space*, *74*(1), 112. https://doi.org/10.1186/s40623-022-01674-7

Heki, K., Bagiya, M. S., & Takasaka, Y. (2022). Slow fault slip signatures in coseismic ionospheric disturbances. *Geophysical Research Letters*, *49*(24), e2022GL101064. https://doi.org/10.1029/2022GL101064

Heki, K. (2021). Chapter 21: Ionospheric disturbances related to earthquakes. In C. Huang, G. Lu, Y. Zhang, & L. J. Paxton (Eds.), *Ionospheric dynamics and applications*, *Geophysical monograph* (pp. 511–526). Wiley/American Geophysical Union. https://doi.org/10.1002/9781119815617.ch21.2021

Heki, K., & Fujimoto, T. (2022). Atmospheric modes excited by the 2021 August eruption of the Fukutoku-Okanoba volcano, Izu-Bonin Arc, observed as harmonic TEC oscillations by QZSS. *Earth Planets and Space*, *74*(1), 27. https://doi.org/10.1186/s40623-022-01587-5

Kherani, E. A., Rolland, L., Lognonne, P., Sladen, A., Klausner, V., & de Paula, E. R. (2016). Traveling ionospheric disturbances propagating ahead of the Tohoku-Oki tsunami: A case study. *Geophysical Journal International*, *204*(2), 1148–1158. https://doi.org/10.1093/gji/ggv500

Li, T., Gao, Y., Chen, C.-H., Zhang, X., & Sun, Y.-Y. (2023). Ionospheric disturbances observed over China after 15 January 2022 Tonga volcan eruption. *Geophysical Journal International*, *273*(1), 909–919. https://doi.org/10.1093/gji/ggad273

Lin, J.-T., Rajesh, P. K., Lin, C. C.-H., Chou, M.-Y., Liu, J.-Y., Yue, J., et al. (2022). Rapid conjugate appearance of the giant ionospheric Lamb wave signatures in the northern hemisphere after Hunga-Tonga volcano eruptions. *Geophysical Research Letters*, *49*(8), e2022GL098222. https://doi.org/10.1029/2022GL098222

Muafiry, I. N., Heki, K., & Maeda, J. (2018). 3D tomography of midlatitude sporadic-E in Japan from GNSS-TEC data. *Earth Planets and Space*, *70*(1), 45. https://doi.org/10.1186/s40623-018-0815-7

Muafiry, I. N., Meilano, I., Heki, K., Wijaya, D. D., & Nugraha, K. A. (2022). Ionospheric disturbances after the 2022 Hunga Tonga-Hunga Ha'apai eruption above Indonesia from GNSS-TEC observations. *Atmosphere*, *13*(10), 1015. https://doi.org/10.3390/atmos13101615

Nakashima, Y., Heki, K., Takeo, A., Cahyadi, M. N., Aditiya, A., & Yoshizawa, K. (2016). Atmospheric resonant oscillations by the 2014 eruption of the Kelud volcano, Indonesia, observed with the ionospheric Total Electron Contents and seismic signal. *Earth and Planetary Science Letters*, *434*, 112–116. https://doi.org/10.1016/j.epsl.2015.11.029

Otsuka, Y., Kotake, N., Shiokawa, K., Ogawa, T., Tsugawa, T., & Saito, A. (2011). Statistical study of medium-scale traveling ionospheric disturbances observed with a GPS receiver network in Japan. In M. A. Abdu, D. Pancheva, & A. Bhattacharyya (Eds.), *Aeronomy of the Earth's atmosphere and ionosphere, vol 291*, *IAGA special Sopron book series 2*.

Rideout, W., & Coster, A. (2006). Automated GPS processing for global total electron content data. *GPS Solutions*, *10*(3), 219–228. https://doi.org/10.1007/s10291-006-0029-5

Tarumi, K., & Yoshizawa, K. (2023). Eruption sequence of the 2022 Hunga Tonga-Hunga Ha'apai explosion from back-projection of teleseismic P waves. *Earth and Planetary Science Letters*, *602*, 117966. https://doi.org/10.1016/j.epsl.2022.117966

Themens, R. T., WatsonŽagar, C. N., Vasylkevych, S., Elvidge, S., McCafrey, A., Prikryl, P., et al. (2022). Global propagation of ionospheric disturbances associated with the 2022 Tonga volcanic eruption. *Geophysical Research Letters*, *49*(7), e2022GL098158. https://doi.org/10.1029/2022GL098158

Wessel, P., Luis, J. F., Uieda, L., Scharroo, R., Wobbe, F., Smith, W. H. F., & Tian, D. (2019). The generic mapping tools version 6 [Software]. Zenodo, *20*, 5556–5564. https://doi.org/10.5281/zenodo.3407866